

GiBS: Generative Input-side Basis-driven Structures

Reza Marzban, Ashkan Zandi, and Ali Adibi*

School of Electrical and Computer Engineering, Georgia Institute of Technology, Atlanta, GA, USA

Abstract

Designing large-scale metasurfaces with nonlocal optical effects remains challenging due to the immense dimensionality and fabrication constraints of conventional optimization methods. We introduce **GiBS** (Generative Input-side Basis-driven Structures), an inverse-design framework that represents the entire device using a compact set of coefficients from smooth parametric bases such as Fourier or Chebyshev functions. This formulation compresses the design space by more than an order of magnitude, enabling efficient optimization of complex, broadband, and aperiodic geometries. GiBS integrates this low-dimensional representation with an autoencoder-based manifold-learning workflow to map the relationship between geometry and optical response, facilitating rapid exploration, discovery of high-performance designs, and systematic analysis of fabrication sensitivity. The inherent smoothness of the basis functions ensures manufacturability while capturing the asymmetry required for nonlocal optical interactions. We experimentally validated the framework through the realization of a PEDOT:PSS broadband scattering metasurface, whose measured response closely matched full-wave simulations across 500–1100 nm. These results establish GiBS as a scalable, data-efficient, and fabrication-aware platform for the inverse design of multifunctional metasurfaces, bridging AI-guided representation learning with experimentally realizable photonic architectures.

1 Introduction

The demand for compact, lightweight, and multifunctional optical components has driven advances in sub-wavelength control of electromagnetic waves. Metasurfaces, planar arrays of engineered nanostructures, provide an alternative to bulk optics and have enabled beam steering [1, 2], lensing and imaging [3, 4], optical neural networks [5, 6, 7], and polarization control [8, 9]. Designing large-area or multifunctional devices, however, remains difficult. The parameter space is immense and non-convex [10], full-wave simulations are costly in time and memory [11], and, critically, the search itself suffers from the curse of dimensionality: even with a fast surrogate, exhaustive or dense exploration of a high-dimensional design space remains infeasible.

A common strategy builds a dictionary of precomputed meta-atoms that are tiled to approximate desired phase or amplitude profiles [8, 12, 13]. This relies on a local periodicity assumption that decouples neighboring responses. The assumption degrades for large deflection angles or strong nonlocal interactions [14], where collective lattice effects and high-Q resonances [15], such as quasi-bound states in the continuum (q-BICs) [16, 17, 18], dominate. Resonant wavelengths can be sensitive to local phase gradients [19], which favors smooth, continuous geometry variations that are not naturally produced by discrete dictionaries [14]. Modern applications further demand multifunctionality, such as distinct behaviors across wavelengths, incident angles, or material states in phase-change systems [20, 21], which places additional strain on discrete catalogs and simple geometries. The combinatorial growth is severe: even a 16×16 array with ten geometric choices per site yields 10^{256} configurations [22], illustrating the fundamental dimensionality bottleneck.

*Corresponding author: ali.adibi@ece.gatech.edu

Gradient-based topological optimization (TO) can generate rich freeform layouts [23], yet it often converges to local optima and requires many random restarts [24, 25]. Multifunctional objectives introduce conflicting gradients, and aggregate metrics, such as worst-case or averaged figures of merit, can trap the optimizer in suboptimal regions [25]. To improve fabrication tolerance, several studies compute three gradients per iteration—nominal, dilation, and erosion—and aggregate them, or introduce projection and smoothing filters to enforce minimum feature sizes and binarization. These steps, while essential for realistic fabrication, increase computational cost and can reduce nominal efficiency if not co-designed with the performance objective. Without them, the realized devices often deviate from simulated performance due to process variations. Purely training-based inverse design models [26, 27, 28, 29] face a different challenge: generating high-quality datasets is expensive, naive sampling produces numerous low-performing structures, and the curse of dimensionality persists even when predictions are fast [25, 30]. Together, these issues motivate a framework that manages dimensionality, incorporates fabrication constraints naturally, and remains data-efficient.

To address these challenges, we look beyond the established geometric parameterizations used in inverse design. These include pixel-based representations, where a device is described on a fine grid with tailored permittivities [31, 23], level-set methods, which define layouts as isocontours of a scalar function [32, 33], explicit shape parameterizations, where analytic functions map a few variables to constrained geometries [34, 35, 36], and neural parameterizations, where layouts are represented by analytic neural networks [37]. Within the broader lens of *input-side representation learning* [30], we propose a fifth class: a global, basis-driven representation. **GiBS (Generative Input-side Basis-driven Structures)** describes the entire device as a continuous function defined by a small set of coefficients in a chosen parametric basis, such as Fourier or Chebyshev series [38, 39]. This smooth, low-dimensional representation directly addresses the need for continuous geometry variations in nonlocal metasurfaces, transforming a combinatorial search into an optimization over a compact, physically interpretable parameter space. Recent findings suggest that even complex freeform devices can be represented by a remarkably small number of latent variables [25], supporting the efficiency and interpretability of the basis-driven approach.

Manufacturability is incorporated at the representation level. Instead of defining arbitrary freeform boundaries, GiBS modulates the parameters of a robust family of primitive shapes, such as nanopillar radii, that are naturally compatible with standard lithographic and etching processes. Simple, convex features are fabricated with higher fidelity and yield [40, 41], whereas complex freeform contours often exhibit reduced reliability [42, 43]. While freeform pipelines can include fabrication-aware steps such as sub-pixel smoothing, projection filters, and minimum-feature constraints, or rely on foundry-compatible workflows [44, 45, 46, 47], these constraints are typically introduced post hoc. GiBS embeds manufacturability by construction through its basis vocabulary, ensuring fabrication-tolerant designs without additional penalty terms [8, 48, 49].

This representation also mitigates the tension between device scale and computational feasibility. Direct pixel optimization of large supercells is intractable [3, 50], whereas local-periodicity approximations neglect long-range coupling [35, 51]. In GiBS, low-order coefficients capture global correlations across the aperture, and higher-order coefficients refine subwavelength details [52], maintaining tractability while preserving physical continuity. This compact description supports multiple optimization pathways. For instance, manifold learning [53] can analyze the latent response manifold generated by different bases, guiding basis selection. The same coefficients can be used in gradient-based shape optimization [36, 54], enabling direct $\partial\text{FoM}/\partial a_k$ updates in a relaxed space with a handful of design variables rather than hundreds of pixels. This not only simplifies the optimization but also enforces manufacturability through its primitive basis functions. Furthermore, fabrication robustness can be assessed by introducing Gaussian perturbations on the coefficients and selecting designs with minimal response deviation. The remainder of this paper presents the theoretical and computational framework of GiBS and concludes with its experimental validation through the design of a wideband transparent beam scatterer.

2 A Parametric Basis Framework for Nonlocal Metasurfaces

2.1 Dimensionality Reduction with Basis Expansions

The core of the GiBS framework is the parameterization of the metasurface geometry using a basis expansion. As illustrated in Figure 1(a–c), this approach replaces discrete meta-atom specification with a continuous functional description of geometric parameters, such as the pillar radius $R(x, y)$. The radius is expressed as a linear combination of orthogonal basis functions $\phi_{n_x, n_y}(x, y)$, governed by a compact set of coefficients a_{n_x, n_y} that define the overall device morphology:

$$R(x, y) = F \left(\sum_{n_x=0}^{N_x} \sum_{n_y=0}^{N_y} a_{n_x, n_y} \phi_{n_x, n_y}(x, y) \right) \quad (1)$$

In Figure 1(a), the table lists the numerical values of representative coefficients for a sample design, while Figure 1(b) visualizes the corresponding nanopillar arrangement within a single supercell. Figure 1(c) extends this configuration to a larger metasurface, demonstrating how continuous variation in the basis coefficients can yield spatially evolving geometries. Together, these panels show how a small set of parameters can encode complex and smoothly varying designs. Here, the coefficients a_{n_x, n_y} serve as the design variables

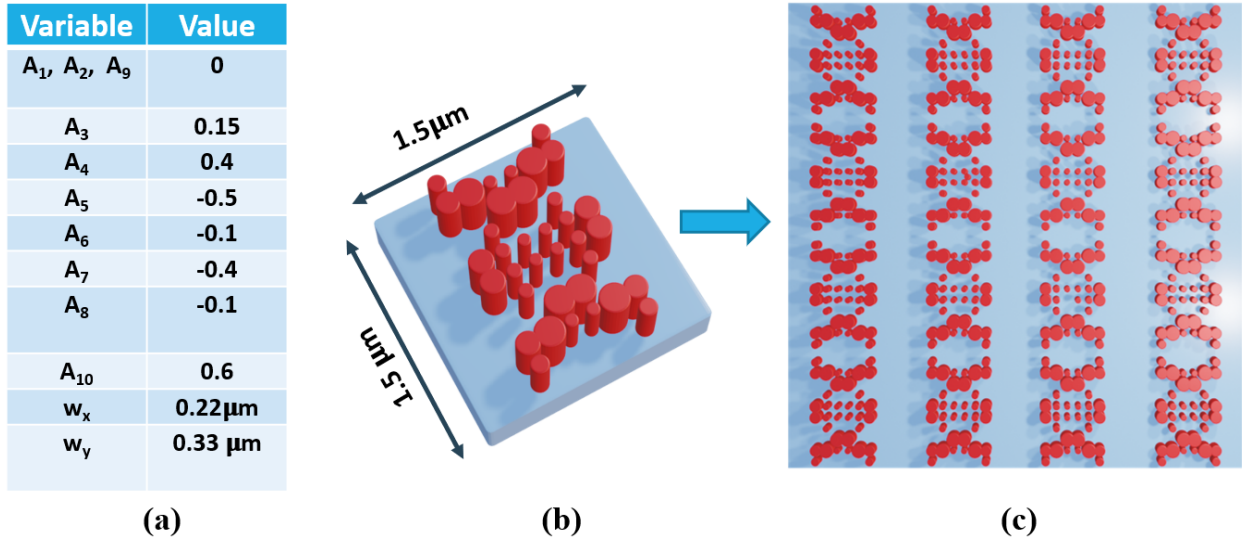


Figure 1: Parametric basis modeling in the GiBS framework. (a) Representative values of the basis coefficients A_k and frequency parameters (ω_x, ω_y) defining the nanopillar distribution. (b) A single supercell geometry generated using these coefficients, showing a smooth and asymmetric variation of pillar radii. (c) Extension of the same pattern to a larger metasurface array, demonstrating how continuous control of the basis terms produces globally varying yet fabrication-friendly layouts.

to be optimized, while $F(\cdot)$ denotes a nonlinear mapping that enforces fabrication constraints, as discussed in Section 2.2. The choice of basis functions ϕ_{n_x, n_y} acts as a structural prior, guiding the model toward geometries that naturally satisfy smoothness and periodicity requirements. In this work, the basis functions control the local radius of cylindrical nanopillars at each point (x, y) ; however, the same formalism can be extended to other unit-cell geometries such as hexagonal posts, rectangular blocks, or even freeform scatterers. Cylindrical pillars were selected in this study because their smooth, edge-free profiles simplify fabrication and mitigate lithographic and etching-induced errors, providing a consistent test platform for validating the framework.

This formulation draws a useful analogy to Rigorous Coupled-Wave Analysis (RCWA), where a known permittivity distribution is expanded into a Fourier series to solve Maxwell's equations [55]. In GiBS, we invert this logic: the basis coefficients themselves become the primary design variables that generate the structure, forming a bridge between the mathematical language of simulation and the optimization process. To illustrate this concept, we employ two representative basis families, Fourier and Chebyshev expansions, which exemplify periodic and finite-aperture configurations, respectively, and collectively demonstrate the generality of the GiBS formulation.

Fourier Basis. A two-dimensional Fourier series provides a natural framework for periodic structures that form the foundation of many metasurfaces. The sinusoidal expansion can be expressed as

$$R(x, y) = r_{\text{base}} \cdot \left(A_0 + \sum_{k=1}^N \left[A_{2k-1} \sin\left(k\omega_x \frac{2\pi x}{P_x} + k\omega_y \frac{2\pi y}{P_y}\right) + A_{2k} \cos\left(k\omega_x \frac{2\pi x}{P_x} + k\omega_y \frac{2\pi y}{P_y}\right) \right] \right), \quad (2)$$

where r_{base} is the base radius, A_k are amplitude coefficients, ω_x and ω_y are spatial frequency parameters, and P_x and P_y are the supercell periodicities. The inherent smoothness of Fourier modes ensures gentle spatial variations, minimizing abrupt phase transitions and promoting stable optical coupling across the aperture.

Chebyshev Basis. For finite-aperture or aperiodic devices, Chebyshev polynomials provide an effective alternative. The Chebyshev polynomials of the first kind, $T_n(u)$, are defined on the interval $[-1, 1]$ by the recurrence relation $T_{n+1}(u) = 2uT_n(u) - T_{n-1}(u)$, with $T_0(u) = 1$ and $T_1(u) = u$. A two-dimensional expansion can then be constructed as

$$\phi_{n_x, n_y}(x, y) = T_{n_x}\left(\frac{2x - (x_{\text{max}} + x_{\text{min}})}{x_{\text{max}} - x_{\text{min}}}\right) T_{n_y}\left(\frac{2y - (y_{\text{max}} + y_{\text{min}})}{y_{\text{max}} - y_{\text{min}}}\right), \quad (3)$$

where the arguments are scaled to map the rectangular domain $[x_{\text{min}}, x_{\text{max}}] \times [y_{\text{min}}, y_{\text{max}}]$ to the canonical square $[-1, 1]^2$. Unlike periodic Fourier series, Chebyshev polynomials emphasize variations near the boundaries, which is advantageous for controlling edge effects and boundary-induced behavior in finite-aperture metasurfaces.

In this work, both Fourier and Chebyshev bases were tested to demonstrate the versatility of the GiBS framework; however, the approach is not limited to these two choices. Other basis families, such as Bessel, Legendre, or wavelet expansions, can be explored for specific applications where the underlying optical modes or physical constraints suggest more suitable functional forms. Selecting or tailoring the basis to match the dominant modal behavior of a given device represents a natural direction for future extensions of this framework.

2.2 Enforcing Asymmetry and Fabrication Constraints

The basis-expansion framework inherently supports asymmetric geometries, which are essential for nonlocal metasurface functionalities such as beam splitting, asymmetric scattering, and polarization conversion. Asymmetry can be introduced naturally by including both sine and cosine components in the Fourier expansion or by incorporating odd-order Chebyshev terms. This enables fine control over spatial phase gradients and coupling pathways without increasing dimensionality.

To bridge the continuous mathematical formulation with the discrete domain of nanofabrication, the GiBS model employs a nonlinear mapping function $F(\cdot)$. This function enforces physical and manufacturing limits, ensuring that generated layouts remain fabrication-compatible. A simple yet effective choice is a

threshold-based rule that suppresses geometrical features below a certain size while preserving the continuous structure of the rest of the design. This operation is particularly useful for lithographic patterning and binary layout generation. One representative form is

$$F(\alpha) = \begin{cases} r_{\text{low}}, & \text{if } \alpha < \theta, \\ \alpha, & \text{otherwise,} \end{cases} \quad (4)$$

where α is the continuous output of the basis expansion, and θ is a tunable threshold that defines the minimum printable feature. In this implementation, when the evaluated radius falls below the threshold, the corresponding pillar is removed (by setting $r_{\text{low}} = 0$), or optionally replaced by a minimum viable radius to retain structural continuity. Values above the threshold remain unchanged, meaning that $R(x, y)$ directly follows the continuous basis expansion for fabricable regions. This selective truncation approach maintains smooth variations where possible while eliminating subwavelength-scale features that cannot be reliably fabricated. By embedding such fabrication awareness directly into the generative model, the optimization explores only physically realizable regions of the design space. This improves convergence efficiency, prevents wasted iterations on non-manufacturable geometries, and enhances the likelihood of experimental success.

2.3 Manifold Learning of Electromagnetic Responses

To demonstrate and evaluate GiBS, we apply it to the inverse design of a broadband scattering metasurface in the conducting polymer PEDOT:PSS [56, 57, 58, 59]. PEDOT:PSS poses a demanding design space: its real refractive index is relatively low in the visible and increases toward the near-infrared, while phase-dependent extinction introduces additional loss in the metallic state [60]. Achieving efficient, wide-angle scattering therefore requires coordinating local resonances (set by nanopillar geometry) with nonlocal, supercell-scale coupling, an optimization that is computationally prohibitive for conventional topology methods or brute-force sweeps over broad spectra. GiBS addresses this challenge by combining low-dimensional geometric encoding with data-driven response modeling. As outlined in Figure 2, basis coefficients specify a supercell (Figure 2b) that is simulated via three-dimensional FDTD (Lumerical) over 400–1200 nm to obtain $\sigma_{\text{abs}}(\lambda)$ and $\sigma_{\text{sca}}(\lambda)$ (Figure 2c). The resulting geometry–response pairs train autoencoders that compress each 201-point spectrum into a compact latent representation (Figure 2d). Reconstructions closely match the simulated spectra (Figure 2e), indicating that the learned latent spaces retain the salient physics of the electromagnetic response.

Architecture and training. For each response type and material phase we train an independent, fully connected, symmetric autoencoder, yielding four models in total: $\{\sigma_{\text{abs}}, \sigma_{\text{sca}}\} \times \{\text{insulator, metal}\}$. Each network takes a 201-point spectrum sampled uniformly over wavelength as input. The encoder maps $\mathbb{R}^{201} \rightarrow \mathbb{R}^2$ through the sequence $201 \rightarrow 90 \rightarrow 60 \rightarrow 50 \rightarrow 20 \rightarrow 2$ using tanh activations, and the decoder mirrors this mapping back to 201 with a linear output layer. The two-dimensional bottleneck enables visualization and clustering of responses while retaining sufficient representational capacity for smooth spectra reconstruction. The model is trained using a combined loss function that balances spectral similarity and amplitude accuracy,

$$\mathcal{L}(y, \hat{y}) = \lambda_1 \left[1 - \frac{y \cdot \hat{y}}{\|y\|_2 \|\hat{y}\|_2} \right] + \lambda_2 \frac{1}{N} \|y - \hat{y}\|_1, \quad \lambda_1 = 0.7, \lambda_2 = 0.3, \quad (5)$$

where y and \hat{y} are the true and reconstructed spectra and $N = 201$. This combination of cosine and absolute losses enforces both phase and magnitude consistency. Each network is trained for 20 epochs on a dataset of 6,000 simulated spectra, with an 80/20 train–test split and validation monitoring. The training set includes three geometry families, random layouts, Fourier-basis GiBS designs, and Chebyshev-basis GiBS designs,

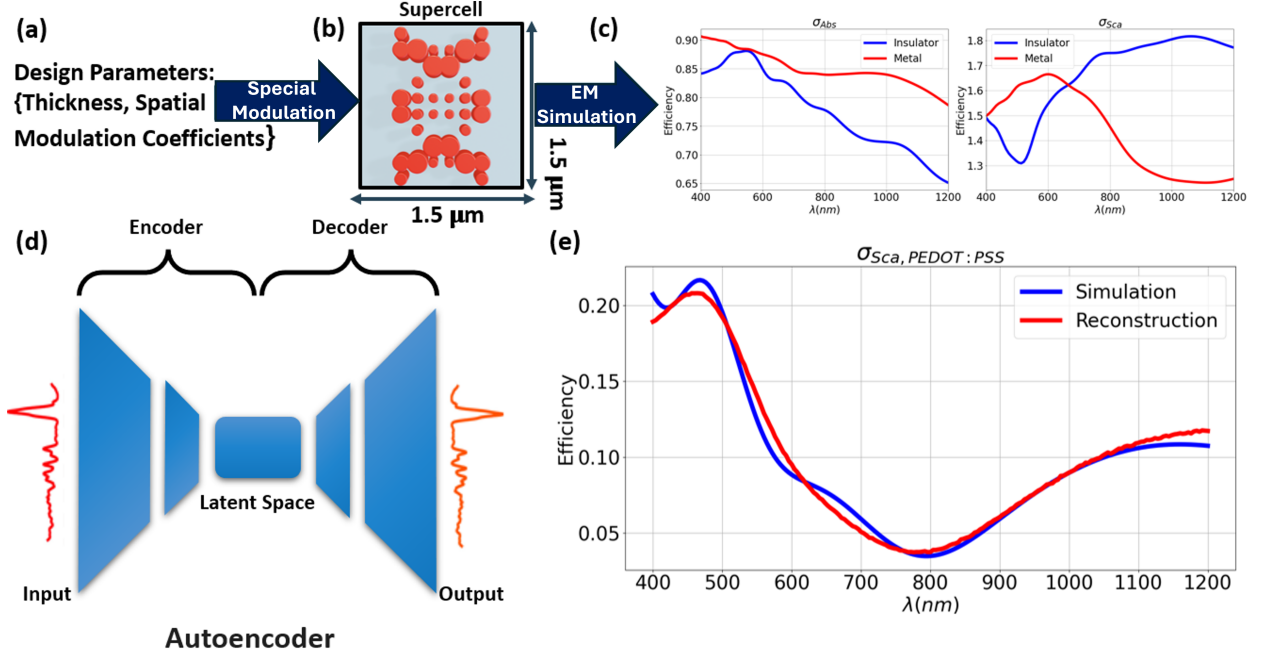


Figure 2: Workflow of the autoencoder-assisted design pipeline. (a) Design parameters (basis coefficients) define (b) a supercell geometry, which is simulated to yield (c) electromagnetic spectra, including both scattering and absorption cross-sections for different material states. (d) One of the trained autoencoders compresses these spectra into a low-dimensional latent space, and (e) reconstructs them with high accuracy, validating the fidelity of the learned manifold. Four separate autoencoders were trained in total, one for each combination of response type (absorption, scattering) and material phase (insulating, metallic). Four independent autoencoders are trained, one per (response, phase) pair.

ensuring the latent manifold captures both structured and unstructured response regimes. The final validation losses converge to the order of 10^{-4} on normalized spectra, consistent with the reconstructions shown in Figure 2e.

This combination of geometric compression (input-side representation) and spectral compression (output-side representation) establishes a closed-loop framework where both the structure and its optical response are embedded in tractable, continuous manifolds. The GiBS representation thus provides the foundation for systematic exploration of nonlocal metasurface behavior in both physical and functional domains.

2.4 Latent Space Analysis for Inverse Design and Active Optics

The learned latent space acts as a navigable map linking geometry to functionality. The autoencoder clusters designs with similar spectral responses close to one another, forming a continuous topology of performance. This organization enables an intuitive inverse design workflow: target optical responses can be associated with regions of the latent manifold, from which new candidate geometries are decoded via their basis coefficients. A key outcome is that the GiBS framework, through its structured basis encoding, substantially enlarges the accessible region of the performance landscape relative to random sampling. As shown in Figure 3a, structures generated by random nanopillar dimensions (red) occupy a compact region of the latent space, whereas those constructed through Fourier (cosine-only, blue) or Chebyshev (green) basis expansions populate a much broader and continuous manifold, corresponding to a richer diversity of spectral behaviors. The two basis families exhibit complementary properties: Fourier bases produce smooth, periodic varia-

tions suited to diffractive or uniformly scattering systems, while Chebyshev bases localize variations near boundaries, enhancing finite-aperture effects and boosting overall scattering strength in the visible region.

Figures 3b and 3c illustrate two representative broadband scatterers selected from high-performing latent regions marked as α and β in Figure 3a. The Fourier (cosine) basis design α exhibits a uniform and balanced scattering response across 400–700 nm, whereas the Chebyshev-based design β produces stronger overall scattering intensity in the visible range. These results demonstrate that different functional bases can yield distinct optical characteristics highlighting the versatility of GiBS in tailoring metasurface behavior through basis selection.

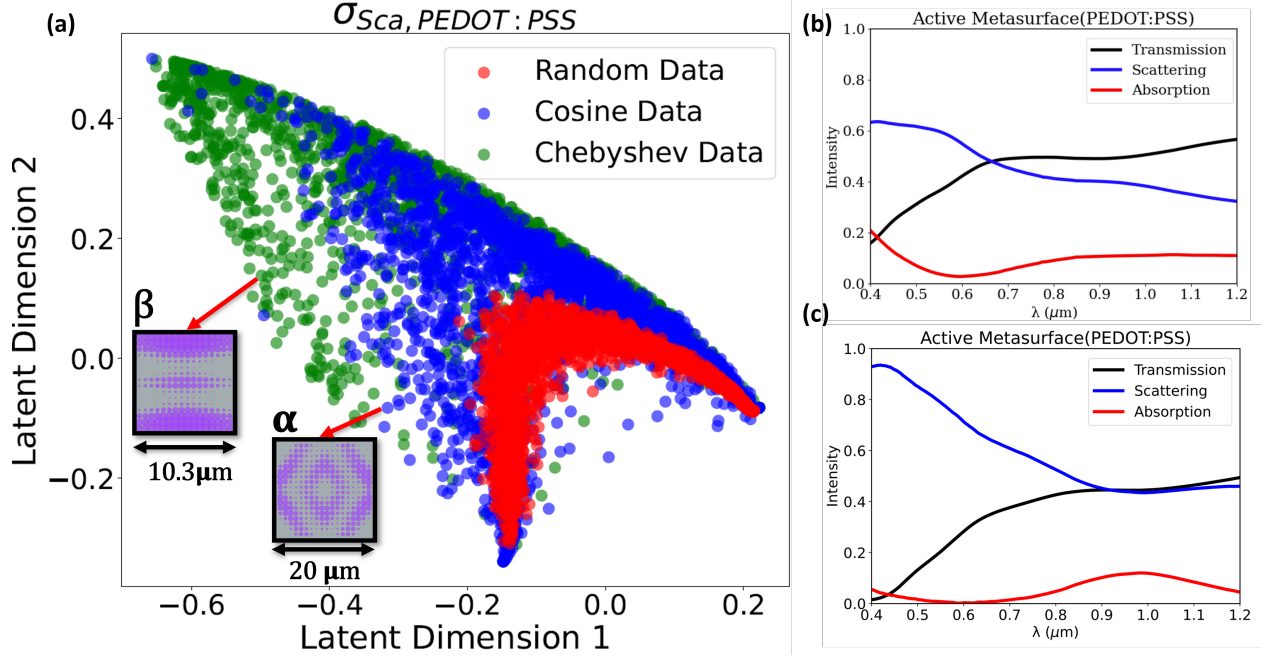


Figure 3: Latent-space analysis of the GiBS framework applied to PEDOT:PSS metasurfaces in the insulating phase. (a) Two-dimensional latent embedding of the scattering cross-sections σ_{sca} showing the distribution of random (red), Fourier cosine (blue), and Chebyshev (green) basis-generated geometries. The Fourier and Chebyshev parameterizations span a broader and more continuous manifold compared to random designs. Insets α and β mark representative 400 nm-thick PEDOT:PSS metasurfaces on SiO_2 substrates with supercell periods of $20\mu m$ and $10.3\mu m$, respectively. (b) Optical response of the Fourier (cosine) basis design α , showing uniform scattering and transmission balance across the visible and near-infrared spectrum. (c) Optical response of the Chebyshev-based design β , exhibiting enhanced scattering intensity in the visible range due to strong boundary modulation. These examples illustrate how different basis functions can generate distinct yet physically consistent electromagnetic responses within the unified GiBS design manifold.

This dual perspective, input-side geometric control via basis coefficients and output-side response analysis via manifold learning, captures the central concept of GiBS. The input representation enforces continuity, manufacturability, and spatially uniform sensitivity to errors, while the learned output manifold organizes the high-dimensional optical response space into interpretable clusters. Together, these elements allow systematic exploration of how geometry, material composition, and tunable parameters govern performance. While the previous section focused on designing broadband scattering in the insulating phase of PEDOT:PSS, the GiBS framework also provides a powerful platform for analyzing and optimizing *active metasurfaces*, systems that exhibit multiple optical states with distinct refractive indices. To illustrate this capability, we

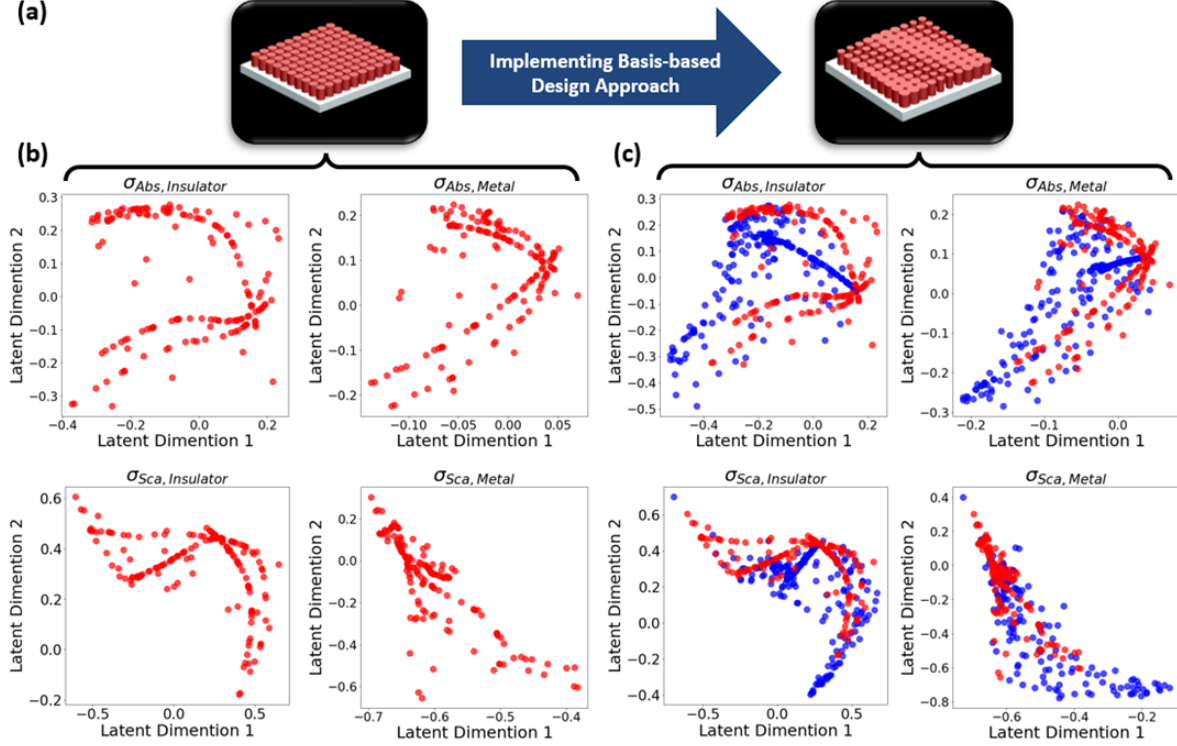


Figure 4: Active-optic design space exploration enabled by the GiBS framework. (a) Schematic illustrating the implementation of the Fourier basis parameterization for 400 nm-thick PEDOT:PSS metasurfaces on SiO_2 , modeled in both insulating and metallic states. (b) Latent embeddings of absorption (σ_{abs}) and scattering (σ_{sca}) spectra for randomly generated geometries, showing limited and disjoint coverage of the response space in both material phases. (c) Corresponding embeddings for GiBS-generated (Fourier basis) designs, where blue points represent basis-driven geometries and red points denote random ones. The structured parameterization provided by GiBS significantly broadens and smooths the latent coverage, revealing continuous and connected manifolds across both insulating and metallic states.

consider a 400 nm-thick PEDOT:PSS film on SiO_2 as a representative active material platform, modeled in both its insulating and metallic phases. The objective here is to simultaneously capture and expand the diversity of responses across both phases, enabling inverse design of metasurfaces that can operate under dual-state objectives. For instance, one may target a design that functions as a strong broadband scatterer in the insulating phase while acting as an efficient absorber in the metallic phase—a configuration that is both spectrally broadband and functionally reconfigurable. As shown in Figure 4, the GiBS framework exhibits a consistent trend of expanding the accessible response space across material states. In this study, the design parameters include both the basis coefficients and the PEDOT:PSS layer thickness, with separate autoencoders trained for the insulating and metallic phases. The schematic in Figure 4a illustrates the implementation of this basis-driven parameterization for both material states. In the random-design case (Figure 4b), the corresponding latent embeddings for both σ_{abs} and σ_{sca} occupy narrow, fragmented regions, indicating that random sampling fails to capture the full diversity of achievable responses in either phase. In contrast, when the geometry is encoded through the Fourier basis representation (Figure 4c), the learned manifolds for both the insulating and metallic states span substantially larger and more continuous regions of the latent space, revealing richer optical behaviors and uncovering new regions of tunability. This expansion of the latent coverage demonstrates that GiBS not only improves the design diversity within a single phase but also provides a unified foundation for dual-state optimization, enabling devices with comple-

mentary functionalities across different material conditions. Once these compact, well-organized manifolds are established, gradient-based or Bayesian optimization methods can be applied to identify Pareto-optimal designs that balance conflicting objectives, such as maximizing scattering in one state while enhancing absorption in another. This integration of structured basis representation with data-driven manifold learning establishes GiBS as a scalable and interpretable framework for active and multifunctional metasurface design. In the following section, we experimentally validate this workflow by fabricating and characterizing a PEDOT:PSS metasurface in its insulating phase, optimized for broadband scattering from 400–1200 nm.

3 Experimental Validation with a PEDOT:PSS Metasurface

To experimentally validate the full GiBS design-to-fabrication workflow, a large-area PEDOT:PSS metasurface was realized on a fused silica (SiO_2) substrate. The optimized design, generated through the GiBS framework, corresponds to a $20\text{ }\mu\text{m} \times 20\text{ }\mu\text{m}$ supercell containing nanopillars with diameters ranging from 80 nm to 900 nm. This parametric distribution enables the coexistence of both local and nonlocal resonances within a single supercell, an essential mechanism for achieving broadband scattering spanning from 500 to 1100 nm. Figure 5 shows scanning electron microscopy (SEM) images of the fabricated structure. The device demonstrates excellent pattern-transfer fidelity, with smooth transitions between adjacent nanopillars and uniform periodicity across the full area. The smallest features (80 nm) and the largest pillars (900 nm) are clearly resolved, confirming the physical realization of the GiBS, optimized geometry. This design serves as an example of how GiBS enables large-scale metastructure optimization that would be prohibitively expensive for traditional TO methods. In a conventional TO workflow, optimizing a device on the scale of $30\lambda \times 30\lambda$ with subwavelength pixel resolution would require handling millions of design variables, leading to extreme memory and computational demands. Moreover, gradient-based TO algorithms are inherently best suited for *many-to-few* mappings, where numerous design parameters target one or a few objective functions. In contrast, broadband metasurface design typically requires simultaneous optimization across hundreds of wavelengths, resulting in a *many-to-many* optimization regime with highly correlated gradients that are difficult to converge. Such constraints render large-scale, broadband TO impractical both computationally and numerically. Similarly, dataset-driven inverse design approaches that rely on random geometric sampling struggle to cover the relevant optical response space, as shown in earlier sections. Randomly generated geometries often yield physically implausible or nonfunctional responses, leading to sparsely populated and discontinuous performance manifolds. The GiBS framework overcomes these limitations by embedding physical priors, through basis expansion and fabrication constraints, directly into the design representation. This ensures that each sampled geometry is both fabrication-feasible and optically meaningful, effectively spanning the space of realizable device responses while maintaining continuity in both geometry and performance.

3.1 Fabrication Process

The fabrication process followed a multi-step protocol to ensure high fidelity and reproducibility. The SiO_2 substrate was first cleaned by sequential rinsing in acetone and isopropyl alcohol (IPA), followed by an oxygen plasma treatment to enhance surface wettability. The PEDOT:PSS film was then deposited using a two-step spin-coating procedure with Heraeus Clevios PH1000 solution, filtered and mixed with IPA to improve uniformity. Each coating was spun at 3000 rpm for 60 s and baked at $120\text{ }^\circ\text{C}$ for 15 min, producing a total film thickness of 400 nm. For patterning, a PMMA A4 resist layer was spin-coated and baked prior to electron-beam lithography (EBL). The optimized GDS file, generated directly from the GiBS parameterization, was written into the resist and developed in a 1:3 mixture of MIBK:IPA. A 30 nm SiO_2 hard mask was then deposited by e-beam evaporation, followed by lift-off in acetone. The pattern was

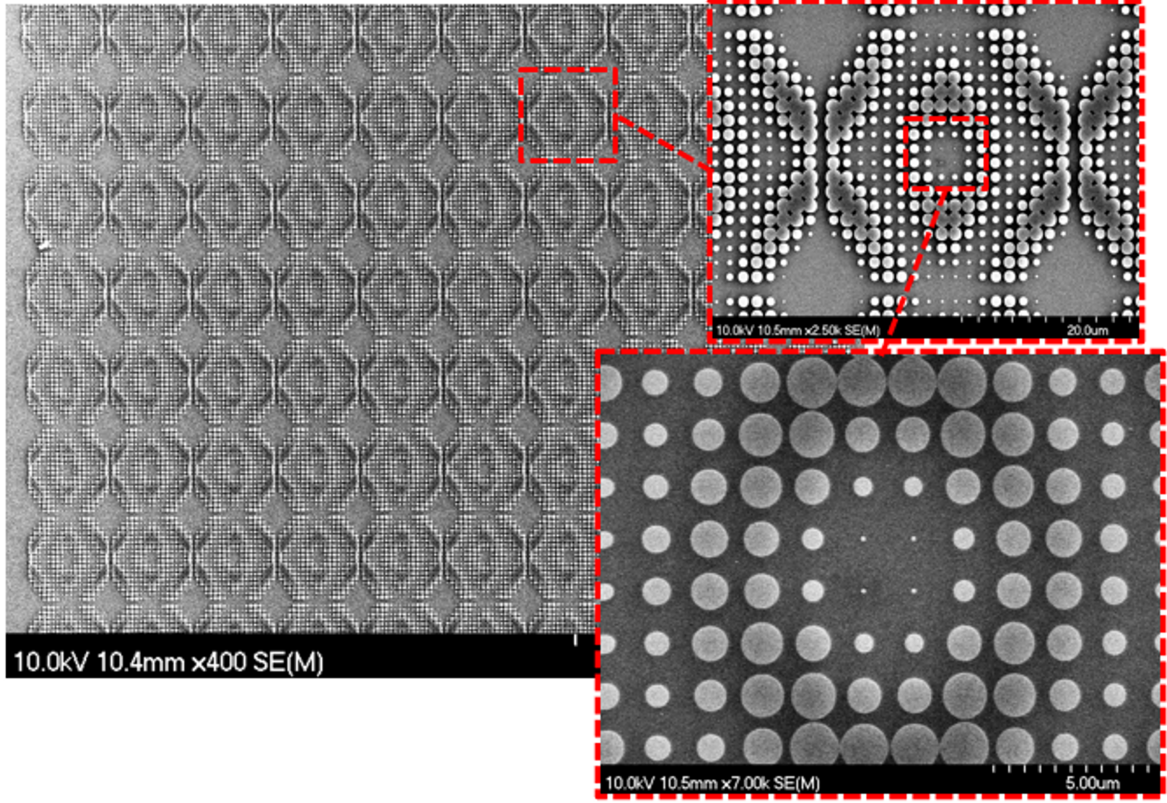


Figure 5: Scanning electron microscope (SEM) images of the fabricated PEDOT:PSS metasurface optimized via the GiBS framework. The device demonstrates large-area periodicity and excellent pattern transfer fidelity, closely matching the designed basis-driven geometry. The structure consists of nanopillars with diameters ranging from 80 nm to 900 nm within a $20\text{ }\mu\text{m} \times 20\text{ }\mu\text{m}$ supercell. The coexistence of these sub- and superwavelength features supports both local and nonlocal resonances, enabling broadband scattering from 500 to 1100 nm. The insets highlight the smooth transitions and uniform feature definition achieved across the 400 nm-thick PEDOT:PSS film.

transferred into the PEDOT:PSS layer using argon dry etching, after which the residual hard mask could be optionally removed using buffered oxide etchant (BOE). SEM imaging (Figure 5) confirmed that the fabricated metasurface accurately reproduces the designed geometry with minimal distortion or collapse.

3.2 Optical Characterization and Results

The optical performance of the fabricated PEDOT:PSS metasurface was characterized using a custom-built, angle-resolved spectroscopy setup. As shown in Figure 6a, the illumination was provided by a SuperK FIANIUM FIU-6 broadband source (NKT Photonics), delivering a high-stability, wide-spectrum output from the visible to near-infrared range. The source beam first passed through an adjustable aperture to define the illumination area and was then directed into the input arm of the setup. After collimation, the beam was focused through an objective lens onto the metasurface sample, which was mounted on a motorized rotation stage. By rotating this stage, the incidence angle on the metasurface could be precisely varied to probe different excitation conditions.

The scattered light was collected using an output arm positioned opposite the input arm, equipped with a fiber-coupled spectrometer (Thorlabs CCS series) mounted on a Newport BGM120CC motorized goniome-

ter. This configuration enabled angular-resolved measurements of the scattered intensity from -45° to $+45^\circ$ relative to the surface normal. The output arm's collection optics were aligned such that the scattered beam was efficiently coupled into the detection fiber and directed to the spectrometer for spectral acquisition. The complete optical path, including the collimation optics, focusing objective, sample stage, and output goniometer, is schematically illustrated in Figure 6b. Each spectrum was recorded relative to a reference SiO_2 substrate under identical illumination conditions to remove the source spectral bias. Multiple scans were averaged, and a moving-average filter was applied to the experimental data to suppress high-frequency noise while retaining the overall spectral evolution. The processed experimental data (solid blue line) are compared with full-wave simulations (dashed blue line) in Figure 6c.

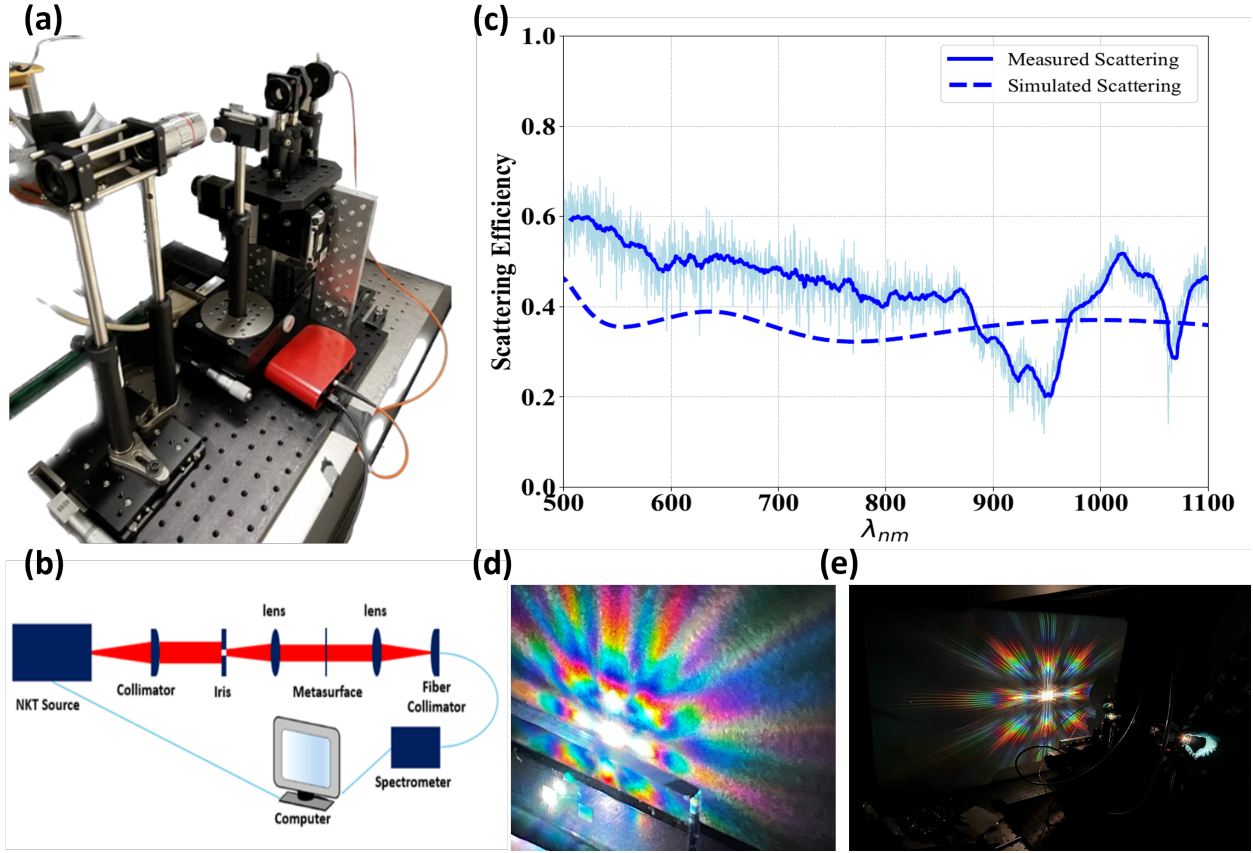


Figure 6: Optical characterization of the fabricated PEDOT:PSS metasurface. (a) Photograph of the custom-built angle-resolved spectroscopy setup used for scattering measurements. (b) Schematic of the optical configuration, showing the SuperK FIANIUM FIU-6 source, collimation optics, metasurface sample mounted on a motorized rotation stage, and the fiber-coupled Thorlabs CCS spectrometer on a Newport BGM120CC motorized goniometer enabling angular scanning from -45° to $+45^\circ$. (c) Comparison of measured (solid blue) and simulated (dashed blue) scattering efficiency spectra. The measured data were post-processed using a moving-average filter to suppress high-frequency noise while preserving broadband features. The slightly higher measured amplitude originates from diffuse and edge scattering effects inherent to the fabricated device. (d) Photograph showing the impact of white-light illumination on the large-scale metastructure. (e) Photographs revealing strong angular scattering under broadband illumination, consistent with the simulated wide-angle response.

Under broadband illumination, the metasurface exhibited vivid, multi-hued scattering across the visible

and near-infrared regions. As shown in Figures. 6d and 6e, white-light illumination produced strong angular dispersion and color separation, confirming the broadband, nonlocal optical behavior designed by the GiBS framework. As shown in Figure 6c, the measured scattering efficiency follows the simulated trend across the 500–1100 nm wavelength range, capturing the principal resonant features and broadband envelope predicted during design. The slightly higher experimental amplitude can be attributed to fabrication-realistic effects that are not captured in idealized full-wave simulations. First, the finite lateral size of the fabricated device ($\sim 200 \times 200 \mu\text{m}^2$) introduces edge diffraction and near-field leakage, which redistribute optical power into the collection cone of the detector. Second, the 400 nm-thick PEDOT:PSS nanopillars exhibit sidewall roughness and minor rounding resulting from etching and solvent reflow, increasing diffuse scattering that adds to the measured intensity but not to the coherent scattering cross section modeled numerically. Third, small refractive-index and thickness inhomogeneities in both the PEDOT:PSS layer and the underlying SiO_2 substrate cause local phase deviations and scattering from interfacial index gradients. Collectively, these effects enhance the total measured signal without altering the overall spectral profile or resonance positions.

The strong spectral correspondence between simulation and experiment confirms that the structures generated by the GiBS inverse-design framework accurately realize the targeted broadband response in practice. By coupling parametric basis representations with latent-space optimization and fabrication-aware constraints, GiBS enables the systematic discovery of large-scale, experimentally feasible metasurfaces that exhibit robust, wideband optical behavior. This result closes the design–fabrication–characterization loop and highlights GiBS as an effective inverse-design route for producing physically consistent, fabrication-tolerant metasurfaces beyond the reach of traditional topology or data-driven optimization approaches.

4 Conclusion

We introduced and experimentally validated the GiBS framework, an inverse-design strategy that integrates parametric basis modeling, representation learning, and fabrication-aware optimization for large-scale, non-local metasurfaces. By replacing discrete, pixel-based representations with continuous basis functions, GiBS compresses the high-dimensional nanophotonic design space into a compact and interpretable form that supports smooth, asymmetric, and aperiodic geometries essential for broadband responses. The latent-space learning module enables efficient exploration of structure–response correlations, while the fabrication-aware parameterization ensures robustness to process-induced variations. The framework was validated through the realization of a broadband scattering metasurface. The fabricated device, consisting of a $20 \mu\text{m} \times 20 \mu\text{m}$ supercell with nanopillars spanning 80–900 nm in diameter, exhibited strong and wide-angle scattering from 500 to 1100 nm. The measured spectra closely matched full-wave simulations, confirming that GiBS-designed structures can faithfully translate inverse-designed geometries into experimentally realizable, high-performance optical components. Beyond this demonstration, GiBS provides a scalable and data-efficient route for hybrid inverse design in nanophotonics. Its flexibility makes it extendable to multilayer and re-configurable systems, while future integration with gradient-informed optimization or active learning could further accelerate convergence and enable multifunctional metasurfaces. Overall, GiBS bridges AI-driven exploration and practical realization, offering a robust pathway toward the next generation of broadband, fabrication-tolerant optical platforms.

Acknowledgments

The authors gratefully acknowledge support from the Georgia Institute of Technology’s Institute for Matter and Systems (IMS).

References

- [1] Sajjad Abdollahramezani, Hossein Taghinejad, Tianren Fan, Mahmood Reza Marzban, Ali A Eftekhari, and Ali Adibi. Reconfigurable multifunctional metasurfaces employing hybrid phase-change plasmonic architecture. *Nanophotonics*, 11(17):3883–3893, 2022.
- [2] Pin Chieh Wu, Ragip A Pala, Ghazaleh Kafaie Shirmanesh, Wen-Hui Cheng, Ruzan Sokhoyan, Meir Grajower, Muhammad Z Alam, Duhyun Lee, and Harry A Atwater. Dynamic beam steering with all-dielectric electro-optic iii–v multiple-quantum-well metasurfaces. *Nature communications*, 10(1):3654, 2019.
- [3] Zhaoyi Li, Raphaël Pestourie, Joon-Suh Park, Yao-Wei Huang, Steven G Johnson, and Federico Capasso. Inverse design enables large-scale high-performance meta-optics reshaping virtual reality. *Nature communications*, 13(1):2409, 2022.
- [4] Zin Lin, Charles Roques-Carmes, Raphaël Pestourie, Marin Soljačić, Arka Majumdar, and Steven G Johnson. End-to-end nanophotonic inverse design for imaging and polarimetry. *Nanophotonics*, 10(3):1177–1187, 2021.
- [5] Tingzhao Fu, Jianfa Zhang, Run Sun, Yuyao Huang, Wei Xu, Sigang Yang, Zhihong Zhu, and Hongwei Chen. Optical neural networks: progress and challenges. *Light: Science & Applications*, 13(1):263, 2024.
- [6] Sanaz Zarei, Mahmood-reza Marzban, and Amin Khavasi. Integrated photonic neural network based on silicon metalines. *Optics Express*, 28(24):36668–36684, 2020.
- [7] Omid Poordashtban, Mahmood Reza Marzabn, and Amin Khavasi. Integrated photonic convolutional neural network based on silicon metalines. *IEEE Access*, 11:61728–61737, 2023.
- [8] Nanfang Yu and Federico Capasso. Flat optics with designer metasurfaces. *Nature materials*, 13(2):139–150, 2014.
- [9] Alexander V Kildishev, Alexandra Boltasseva, and Vladimir M Shalaev. Planar photonics with metasurfaces. *Science*, 339(6125):1232009, 2013.
- [10] Abdourahman Khairreh-Walieh, Denis Langevin, Pauline Bennet, Olivier Teytaud, Antoine Moreau, and Peter R Wiecha. A newcomer’s guide to deep learning for inverse design in nano-photonics. *Nanophotonics*, 12(24):4387–4414, 2023.
- [11] Sean Molesky, Zin Lin, Alexander Y Piggott, Weiliang Jin, Jelena Vucković, and Alejandro W Rodriguez. Inverse design in nanophotonics. *Nature Photonics*, 12(11):659–670, 2018.
- [12] Ata Chizari, Sajjad Abdollahramezani, Mohammad Vahid Jamali, and Jawad A Salehi. Analog optical computing based on a dielectric meta-reflect array. *Optics letters*, 41(15):3451–3454, 2016.
- [13] Sajjad Abdollahramezani, Omid Hemmatyar, and Ali Adibi. Meta-optics for spatial optical analog computing. *Nanophotonics*, 9(13):4075–4095, 2020.
- [14] Christina Spägle, Michele Tamagnone, Dmitry Kazakov, Marcus Ossiander, Marco Piccardo, and Federico Capasso. Multifunctional wide-angle optics and lasing based on supercell metasurfaces. *Nature communications*, 12(1):3787, 2021.

- [15] Kirill Koshelev, Sergey Lepeshov, Mingkai Liu, Andrey Bogdanov, and Yuri Kivshar. Asymmetric metasurfaces with high-q resonances governed by bound states in the continuum. *Physical review letters*, 121(19):193903, 2018.
- [16] Thanh Xuan Hoang, Daniel Leykam, Hong-Son Chu, Ching Eng Png, Francisco J García-Vidal, and Yuri S Kivshar. Collective nature of high-q resonances in finite-size photonic metastructures. *Physical Review Research*, 7(1):013316, 2025.
- [17] Chia Wei Hsu, Bo Zhen, A Douglas Stone, John D Joannopoulos, and Marin Soljačić. Bound states in the continuum. *Nature Reviews Materials*, 1(9):1–13, 2016.
- [18] Adam Overvig and Andrea Alù. Wavefront-selective fano resonant metasurfaces. *Advanced Photonics*, 3(2):026002–026002, 2021.
- [19] Stephanie C Malek, Adam C Overvig, Andrea Alù, and Nanfang Yu. Multifunctional resonant wavefront-shaping meta-optics based on multilayer and multi-perturbation nonlocal metasurfaces. *Light: Science & Applications*, 11(1):246, 2022.
- [20] Omid Hemmatyar, Sajjad Abdollahramezani, Ioannis Zeimpekis, Sergey Lepeshov, Alex Krasnok, Asir Intisar Khan, Kathryn M Neilson, Christian Teichrib, Tyler Brown, Eric Pop, et al. Enhanced meta-displays using advanced phase-change materials. *arXiv preprint arXiv:2107.12159*, 2021.
- [21] Reza Marzban, Nattakorn Kittisut, Ashkan Zandi, Hamed Abiri, and Ali Adibi. Inverse design of optimal metaphotonic devices for dynamic structural colors using physics-informed neural networks. In *Photonic and Phononic Properties of Engineered Nanostructures XV*, page PC133770U. SPIE, 2025.
- [22] Yashar Kiarashinejad, Sajjad Abdollahramezani, Mohammadreza Zandehshahvar, Omid Hemmatyar, and Ali Adibi. Deep learning reveals underlying physics of light–matter interactions in nanophotonic devices. *Advanced Theory and Simulations*, 2(9):1900088, 2019.
- [23] Jakob Søndergaard Jensen and Ole Sigmund. Topology optimization for nano-photonics. *Laser & Photonics Reviews*, 5(2):308–321, 2011.
- [24] Rasmus E Christiansen and Ole Sigmund. Inverse design in photonics by topology optimization: tutorial. *Journal of the Optical Society of America B*, 38(2):496–509, 2021.
- [25] Reza Marzban, Hamed Abiri, Raphaël Pestourie, and Ali Adibi. Hilab: A hybrid inverse-design framework. *Small Methods*, page e00975, 2025.
- [26] Yashar Kiarashinejad, Sajjad Abdollahramezani, and Ali Adibi. Deep learning approach based on dimensionality reduction for designing electromagnetic nanostructures. *npj Computational Materials*, 6(1):12, 2020.
- [27] Zhaocheng Liu, Dayu Zhu, Sean P Rodrigues, Kyu-Tae Lee, and Wenshan Cai. Generative model for the inverse design of metasurfaces. *Nano letters*, 18(10):6570–6576, 2018.
- [28] Sensong An, Clayton Fowler, Bowen Zheng, Mikhail Y Shalaginov, Hong Tang, Hang Li, Li Zhou, Jun Ding, Anuradha Murthy Agarwal, Clara Rivero-Baleine, et al. A deep learning approach for objective-driven all-dielectric metasurface design. *Acs Photonics*, 6(12):3196–3207, 2019.
- [29] Yashar Kiarashinejad, Mohammadreza Zandehshahvar, Sajjad Abdollahramezani, Omid Hemmatyar, Reza Pourabolghasem, and Ali Adibi. Knowledge discovery in nanophotonics using geometric deep learning. *Advanced Intelligent Systems*, 2(2):1900132, 2020.

- [30] Reza Marzban, Ali Adibi, and Raphael Pestourie. Inverse design in nanophotonics via representation learning. *arXiv preprint arXiv:2507.00546*, 2025.
- [31] Alexander Y Piggott, Jesse Lu, Konstantinos G Lagoudakis, Jan Petykiewicz, Thomas M Babinec, and Jelena Vučković. Inverse design and demonstration of a compact and broadband on-chip wavelength demultiplexer. *Nature photonics*, 9(6):374–377, 2015.
- [32] Stanley Osher and James A Sethian. Fronts propagating with curvature-dependent speed: Algorithms based on hamilton-jacobi formulations. *Journal of computational physics*, 79(1):12–49, 1988.
- [33] Michael Yu Wang, Xiaoming Wang, and Dongming Guo. A level set method for structural topology optimization. *Computer methods in applied mechanics and engineering*, 192(1-2):227–246, 2003.
- [34] Mingkun Chen, Jiaqi Jiang, and Jonathan A Fan. Design space reparameterization enforces hard geometric constraints in inverse-designed nanophotonic devices. *ACS Photonics*, 7(11):3141–3151, 2020.
- [35] You Zhou, Yixuan Shao, Chenkai Mao, and Jonathan A Fan. Inverse-designed metasurfaces with facile fabrication parameters. *Journal of Optics*, 26(5):055101, 2024.
- [36] Erez Gershgnabel, Mingkun Chen, Chenkai Mao, Evan W Wang, Philippe Lalanne, and Jonathan A Fan. Reparameterization approach to gradient-based inverse design of three-dimensional nanophotonic devices. *ACS Photonics*, 10(4):815–823, 2022.
- [37] Tianxiang Dai, Yixuan Shao, Chenkai Mao, Yu Wu, Sara Azzouz, You Zhou, and Jonathan A Fan. Shaping freeform nanophotonic devices with geometric neural parameterization. *npj Computational Materials*, 11(1):259, 2025.
- [38] MG Moharam and Thomas K Gaylord. Rigorous coupled-wave analysis of planar-grating diffraction. *Journal of the Optical Society of America*, 71(7):811–818, 1981.
- [39] Govind P Agrawal. *Fiber-optic communication systems*. John Wiley & Sons, 2012.
- [40] Mohammadreza Khorasaninejad, Wei Ting Chen, Robert C Devlin, Jaewon Oh, Alexander Y Zhu, and Federico Capasso. Metalenses at visible wavelengths: Diffraction-limited focusing and subwavelength resolution imaging. *Science*, 352(6290):1190–1194, 2016.
- [41] Amir Arbabi, Yu Horie, Alexander J Ball, Mahmood Bagheri, and Andrei Faraon. Subwavelength-thick lenses with high numerical apertures and large efficiency based on high-contrast transmitarrays. *Nature communications*, 6(1):7069, 2015.
- [42] Martin F Schubert, Alfred KC Cheung, Ian AD Williamson, Aleksandra Spyra, and David H Alexander. Inverse design of photonic devices with strict foundry fabrication constraints. *ACS Photonics*, 9(7):2327–2336, 2022.
- [43] Raphaël Pestourie, Carlos Pérez-Arancibia, Zin Lin, Wonseok Shin, Federico Capasso, and Steven G Johnson. Inverse design of large-area metasurfaces. *Optics express*, 26(26):33732–33747, 2018.
- [44] Alec M Hammond, Ardavan Oskooi, Ian M Hammond, Mo Chen, Stephen E Ralph, and Steven G Johnson. Unifying and accelerating level-set and density-based topology optimization by subpixel-smoothed projection. *Optics Express*, 33(16):33620–33642, 2025.
- [45] Yixuan Pan, Xing Zhang, Kevin Zhu, Philipp Fath, Jiaji Hu, and Jelena Vuckovic. Fabrication tolerant multi-layer integrated photonic topology optimization. *APL Photonics*, 8(8), 2023.

- [46] Bong Hwan Kim, Haejun Chung, Chanik Kang, Chaejin Park, and Min Seok Jang. Low-loss high-density inverse-designed structures for high power signal routing on integrated silicon photonics foundry platforms. *Advanced Optical Materials*, 12(15):2301188, 2024.
- [47] Mo Chen, Ka Fai Chan, Alec M Hammond, Chi-Hou Chan, and Steven G Johnson. Inverse design of 3d-printable metalenses with complementary dispersion for terahertz imaging. *ACS Photonics*, 2025.
- [48] Qiong He, Shulin Sun, Shiyi Xiao, and Lei Zhou. High-efficiency metasurfaces: principles, realizations, and applications. *Advanced Optical Materials*, 6(19):1800415, 2018.
- [49] Yuheng Chen, Alexander Montes McNeil, Taehyuk Park, Blake A Wilson, Vaishnavi Iyer, Michael Bezick, Jae-Ik Choi, Rohan Ojha, Pravin Mahendran, Daksh Kumar Singh, et al. Machine-learning-assisted photonic device development: a multiscale approach from theory to characterization. *Nanophotonics*, (0), 2025.
- [50] Chanik Kang, Chaejin Park, Myunghoo Lee, Joonho Kang, Min Seok Jang, and Haejun Chung. Large-scale photonic inverse design: computational challenges and breakthroughs. *Nanophotonics*, 13(20):3765–3792, 2024.
- [51] Guanghao Chen, Zachary Burns, Junxiao Zhou, and Zhaowei Liu. Inverse design of metasurface based off-axis image relay. *Optics Express*, 32(9):15115–15125, 2024.
- [52] Yujiao Bi, Yuechun Shi, and Zhanghua Han. Spatial-dispersioned nonlocal metasurfaces with angular interrogation: An efficient alternative to surface plasmon resonances for the characterization of biomolecule interactions. *APL Photonics*, 10(3), 2025.
- [53] Mohammadreza Zandehshahvar, Yashar Kiarashinejad, Muliang Zhu, Hossein Maleki, Tyler Brown, and Ali Adibi. Manifold learning for knowledge discovery and intelligent inverse design of photonic nanostructures: breaking the geometric complexity. *Acs Photonics*, 9(2):714–721, 2022.
- [54] Andrew S Thelen, Dean E Bryson, Bret K Stanford, and Philip S Beran. Multi-fidelity gradient-based optimization for high-dimensional aeroelastic configurations. *Algorithms*, 15(4):131, 2022.
- [55] MG Moharam, Drew A Pommet, Eric B Grann, and Thomas K Gaylord. Stable implementation of the rigorous coupled-wave analysis for surface-relief gratings: enhanced transmittance matrix approach. *Journal of the Optical Society of America A*, 12(5):1077–1086, 1995.
- [56] Xi Fan, Wanyi Nie, Hsinhan Tsai, Naixiang Wang, Huihui Huang, Yajun Cheng, Rongjiang Wen, Liujia Ma, Feng Yan, and Yonggao Xia. Pedot: Pss for flexible and stretchable electronics: modifications, strategies, and applications. *Advanced Science*, 6(19):1900813, 2019.
- [57] Siddharth Doshi, Dominik Ludescher, Julian Karst, Moritz Floess, Johan Carlström, Bohan Li, No-far Mintz Hemed, Yi-Shiou Duh, Nicholas A Melosh, Mario Hentschel, et al. Direct electron beam patterning of electro-optically active pedot: Pss. *Nanophotonics*, 13(12):2271–2280, 2024.
- [58] Dominik Ludescher, Pavel Ruchka, Leander Siegle, Yanzhe Huang, Philipp Flad, Monika Ubl, Sabine Ludwigs, Mario Hentschel, and Harald Giessen. Femtosecond direct laser writing of conductive and electrically switchable pedot: Pss optical nanostructures. *Advanced Optical Materials*, 13(15):2403271, 2025.
- [59] Yohan Lee, Julian Karst, Monika Ubl, Mario Hentschel, and Harald Giessen. Dynamic beam control based on electrically switchable nanogratings from conducting polymers. *Nanophotonics*, 12(14):2865–2871, 2023.

- [60] Carsten Dingler, Ramon Walter, Bruno Gompf, and Sabine Ludwigs. In situ monitoring of optical constants, conductivity, and swelling of PEDOT:PSS from doped to the fully neutral state. *Macromolecules*, 55(5):1600–1608, 2022.